

Subcompartmentalization of polyampholyte species in organelle-like condensates is promoted by charge pattern mismatch and strong excluded-volume interaction

Tanmoy Pal,¹ Jonas Wessén,¹ Suman Das,¹ and Hue Sun Chan^{1,*}

¹*Department of Biochemistry, University of Toronto,
Toronto, Ontario M5S 1A8, Canada*

(Dated: June 23, 2020)

Abstract

Polyampholyte field theory and explicit-chain molecular dynamics models of sequence-specific phase separation of a system with two intrinsically disordered protein (IDP) species indicate consistently that a substantial polymer excluded volume and a significant mismatch of the IDP sequence charge patterns can act in concert, but not in isolation, to demix the two IDP species upon condensation. This finding reveals an energetic-geometric interplay in a stochastic, “fuzzy” molecular recognition mechanism that may facilitate subcompartmentalization of membraneless organelles.

Introduction.—Liquid-liquid phase separation (LLPS) [1–5] in biomolecular condensates [6] has garnered intense interest in diverse areas of biomedicine, biophysics, and polymer physics [7]. In the cellular environment, LLPS is a significant factor in the assembly of compartments, sometimes referred to as membraneless organelles, that act as hubs for biochemical processes and physiological regulation. These droplet-like structures coexist with a more dilute milieu. Examples include nucleoli, P-bodies, stress granules, cajal bodies, in an expanding list due to rapid experimental advance. Biomolecular condensates are critical for organismal function and thus their misregulation can cause diseases such as Alzheimer’s, Parkinson’s and amyotrophic lateral sclerosis [8, 9].

Functional biomolecular LLPS often involves intrinsically disordered proteins (IDPs) and nucleic acids engaging in multivalent interactions [10, 11]. Although much remains to be elucidated, recent theories and computations have shed light on the physics of how LLPSs of IDPs are governed by their amino acid sequences. These efforts include analytical theory [12–14], explicit-chain lattice [15–17] and continuum molecular dynamics (MD) [18–20] simulations, and field-theoretic simulation (FTS) [21–23] of LLPS, investigations of the relationship between LLPS propensity and single/double-chain properties [24, 25] as well as crystals and filaments formation [26], and studies of the peculiar temperature [27] and pressure [28] dependence of biomolecular LLPS as well as finite-size scaling in droplet formation [29]. Reviews of the emerging theoretical perspectives are available in Refs. [30–34].

IDPs are enriched in charged and polar residues [35] and multivalent electrostatics is an important driving force—among others [36]—for LLPS. One consistent finding from theory [12], chain simulation [16, 19] and FTS [22, 23] is that the LLPS propensity of a polyampholyte depends on its sequence charge pattern, which may be quantified by an intuitive blockiness κ measure [37] or an analytic “sequence charge decoration” (SCD) parameter [38] that correlates with single-chain properties [37–39]. This perspective was applied to provide a quantitative account [12] for the LLPS of RNA helicase Ddx4 [5].

In contrast to simple laboratory systems that may contain only one IDP type (species), large numbers of different types of IDPs and other biomolecules interact in the cell while compartmentalizing into a variety of different condensates. For some membraneless organelles, LLPS-mediated organization of intracellular space goes a step further by subcompartmentalization [40]. Well-known examples include the nucleolus comprising of at least three subcompartments enriched with distinct sets of proteins [15, 41] and stress granules with

a dense core surrounded by a liquid-like outer shell [42]. These phenomena of IDP compartmentalization *and* subcompartmentalization raise intriguing physics questions as to the nature of the sequence-specific interactions that drive a subset of IDPs in a condensate to coalesce among themselves while excluding other types of IDPs.

Important insights into formation of subcompartments [15, 43] and general principles of many-component phase behaviors [44] have been gained from simulated lattice systems with energies assigned to favor or disfavor pairwise interactions between specific solute components. These approaches do not address, however, how those interactions arise from elementary physical forces in a sequence-dependent manner. The first attempt to tackle this fundamental question uses random phase approximation (RPA) [12, 45] to model LLPS of two polyampholytic IDP species. Sequence-specific molecular recognition is seen as arising from elementary electrostatic interactions in a stochastic, “fuzzy” manner, in that the IDP species are predicted to demix upon LLPS when their sequence charge patterns are significantly different (large difference in their SCD values), but tend to be miscible when their SCD values are similar [46].

TABLE I. Hamiltonians used in this work; $\beta=k_{\text{B}}T$, where k_{B} is Boltzmann’s constant and T is absolute temperature.

	\hat{H}_0	\hat{H}_1	\hat{H}_2
FTS:	$\frac{3}{2b^2\beta} \sum_{p,i,\alpha} \mathbf{r}_{p,i,\alpha+1} - \mathbf{r}_{p,i,\alpha} ^2$	$\frac{v}{2\beta} \int d\mathbf{r} \int d\mathbf{r}' \hat{\rho}_{\text{b}}(\mathbf{r}) \delta(\mathbf{r} - \mathbf{r}') \hat{\rho}_{\text{b}}(\mathbf{r}')$	$\frac{l_{\text{B}}}{2\beta} \int d\mathbf{r} \int d\mathbf{r}' \frac{\hat{\rho}_{\text{c}}(\mathbf{r}) \hat{\rho}_{\text{c}}(\mathbf{r}')}{ \mathbf{r} - \mathbf{r}' }$
MD:	$\frac{K_{\text{b}}}{2} \sum_{p,i,\alpha} (\mathbf{r}_{p,i,\alpha+1} - \mathbf{r}_{p,i,\alpha} - a_0)^2$	$\frac{2\epsilon}{3} \sum_{\substack{p,i,\alpha, \\ \neq q,j,\gamma}} \left[\left(\frac{r_0}{ \mathbf{r}_{p,i,\alpha} - \mathbf{r}_{q,j,\gamma} } \right)^{12} - \left(\frac{r_0}{ \mathbf{r}_{p,i,\alpha} - \mathbf{r}_{q,j,\gamma} } \right)^6 \right]$	$\frac{l_{\text{B}}}{2\beta} \sum_{\substack{p,i,\alpha, \\ \neq q,j,\gamma}} \frac{\sigma_{p,\alpha} \sigma_{q,\gamma}}{ \mathbf{r}_{p,i,\alpha} - \mathbf{r}_{q,j,\gamma} }$

Nonetheless, a definitive delineation of the roles of sequence charge pattern and polymer excluded volume in the mixing/demixing of polyampholytes upon LLPS is yet to be achieved because bead-bead excluded volume was not fully accounted for in RPA [46] and comparisons with explicit-chain MD suggest that diminished excluded volume can lead to artefactually high LLPS propensity [19]. In this Letter, these issues are elucidated using complementary methods of FTS and MD to model polyampholytes with short-range excluded volume repulsion and long-range Coulomb interaction. By construction, FTS is more accurate than RPA in the field-theoretic context if discretization and finite-volume errors can be neglected, whereas MD is more suitable for chemically realistic interactions and its microscopic structural information is accessible. Although our models are both

highly coarse-grained, the collective behaviors studied are not expected to be too sensitive to microscopic details. Surprisingly, both models indicate that while charge pattern mismatch is necessary for polyampholyte demixing, the degree of demixing is highly sensitive to the excluded-volume interaction strength, underscoring that excluded volume is a critical organizing principle not only for folded protein structures [47, 48] and disordered protein conformations [49–51] but also for biomolecular condensates.

Here we study binary mixtures of two species of fully charged, overall neutral bead-spring polyampholytes differing only in their charge patterns, defined by the set of positions $\mathbf{r}_{p,i,\alpha}$ of bead α on chain i of type (species) p with corresponding electric charges $\sigma_{p,\alpha}$ for all i . The sequences considered (Fig. 1) are representative of the set of 50mer “sv sequences”, used extensively for modeling [22, 24, 38, 46], that are listed in ascending κ values from the least blocky, strictly alternating sv1 to the most blocky diblock sequence sv30 [37]. The FTS and MD Hamiltonians, $\hat{H}=\hat{H}_0+\hat{H}_1+\hat{H}_2$, are given in Table I. The chain connectivity term \hat{H}_0 takes the usual Gaussian form with Kuhn length b for FTS and the harmonic form with force constant K_b for MD (thus b corresponds to a_0); the excluded-volume term \hat{H}_1 entails a δ -function with strength v for FTS [22, 52] and a Lennard-Jones (LJ) potential with well depth $\epsilon/3$ for MD [19]; whereas electrostatics is provided by \hat{H}_2 with Bjerrum length l_B .

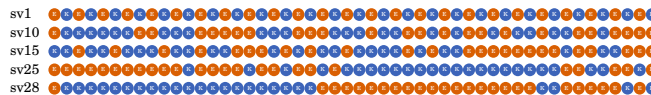


FIG. 1. Polyampholytes studied in this work. Blue/red beads of “K”s (lysines)/“E”s (glutamic acids) carry ± 1 protonic charges. The sv labels are those of Ref. [37].

FTS.—The FTS interaction strengths are controlled by v and l_B (Table I). Following standard prescription, we express \hat{H}_1 and \hat{H}_2 in terms of $\hat{\rho}_b(\mathbf{r})=\sum_p\hat{\rho}_{b,p}(\mathbf{r})$, $\hat{\rho}_c(\mathbf{r})=\sum_p\hat{\rho}_{c,p}(\mathbf{r})$ where $\hat{\rho}_{b,p}$ and $\hat{\rho}_{c,p}$ are, respectively, the microscopic bead (matter) and charge densities of polymer type p . The individual beads are modelled as normalized Gaussian distributions $\Gamma(\mathbf{r})=\exp(-\mathbf{r}^2/2a^2)/(2\pi a^2)^{3/2}$ centered at positions $\mathbf{r}_{p,i,\alpha}$ [53, 54] such that $\hat{\rho}_{b,p}(\mathbf{r})=\sum_{i,\alpha}\Gamma(\mathbf{r}-\mathbf{r}_{p,i,\alpha})$, $\hat{\rho}_{c,p}(\mathbf{r})=\sum_{i,\alpha}\sigma_{p,\alpha}\Gamma(\mathbf{r}-\mathbf{r}_{p,i,\alpha})$. As in recent works [21, 22], we set the smearing length $a=b/\sqrt{6}$.

The canonical partition function for this system can be converted, through standard

methods (see e.g. [55]), to that of a statistical field theory with Hamiltonian

$$H[w, \Phi] = \frac{1}{\beta_F} \left\{ - \sum_p n_p \ln Q_p[\mathbf{i}\check{w}, \mathbf{i}\check{\Phi}] + \int d\mathbf{r} \left(\frac{w^2}{2v} + \frac{(\nabla \Phi)^2}{8\pi l_B} \right) \right\}, \quad (1)$$

where β_F ($\neq \beta$) is the reciprocal temperature in the field picture, n_p is the number of molecules of type p in the system, $\mathbf{i}^2 = -1$. Here $Q_p[\mathbf{i}\check{w}, \mathbf{i}\check{\Phi}]$ is the partition function of a single polymer of type p , subject to external chemical and electrostatic potential fields $\mathbf{i}\check{w} \equiv \Gamma \star \mathbf{i}w$ and $\mathbf{i}\check{\Phi} \equiv \Gamma \star \mathbf{i}\Phi$, respectively, with ‘ \star ’ denoting spatial convolution.

In our lattice simulations of this system, the continuum fields are approximated by discrete field variables defined on a simple cubic lattice (mesh) with periodic boundary conditions. Equilibrium dynamics entailed by $\beta_F H[w, \Phi]$ is simulated using a Complex-Langevin (CL) prescription [56–59], with CL-time evolution governed by $\partial \varphi(\mathbf{r}, t) / \partial t = -\delta \beta_F H / \delta \varphi(\mathbf{r}, t) + \eta_\varphi(\mathbf{r}, t)$ for $\varphi = w, \Phi$, which we integrate numerically using the first-order semi-implicit method of [60] with an appropriate real-valued Gaussian noise η_φ , and ensemble averages, $\langle \dots \rangle$, are computed as asymptotic CL-time averages.

Because the bead positions $\mathbf{r}_{p,i,\alpha}$ are traded in FTS for the $w(\mathbf{r})$, $\Phi(\mathbf{r})$ fields as thermodynamic degrees of freedom, information about spatial structure of the chains has to be gleaned from functionals of $\{\hat{\rho}_{b,p}\}$, with well-defined corresponding field operators, such as the pair-distribution functions (PDFs),

$$G_{p,q}(|\mathbf{r} - \mathbf{r}'|) = \langle \hat{\rho}_{b,p}(\mathbf{r}) \hat{\rho}_{b,q}(\mathbf{r}') \rangle, \quad (2)$$

between various p, q bead types. Both inter- ($p \neq q$) and intra ($p = q$) species PDFs are needed to characterize structural organization of different species. For instance, an intra species $G_{p,p}(r)$ peaking at small r and decays to 0 at large r implies a relatively dense region, i.e., a droplet, of p ; and demixing of two species p and q is signalled by $G_{p,p}(r)$ and $G_{q,q}(r)$ dominating over $G_{p,q}(r)$ at small r .

We examine systematically the interplay of charge pattern and excluded volume in the mixing/demixing of phase-separated polyampholytes by FTS of binary mixtures of four sequence pairs with $p = \text{sv28}$ ($-\text{SCD} = 15.99$), $q = \text{sv1}, \text{sv10}, \text{sv15}, \text{sv25}$ ($-\text{SCD} = 0.41, 2.10, 4.35, 12.77$), bulk monomer densities $\rho_p^0 = \rho_q^0 = 0.25b^{-3}$ and a large $l_B = 5b$ to ensure LLPS in all cases, each at excluded-volume strengths $v/b^3 = 0.0068, 0.034, 0.068$ and 0.102 . The

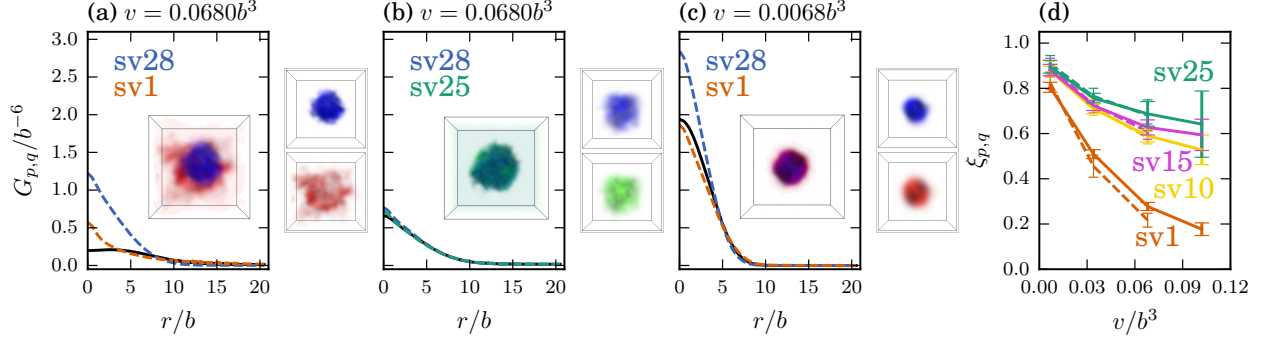


FIG. 2. FTS-computed PDFs and mixing parameter $\xi_{p,q}$ for binary sv sequence mixtures. (a–c) Each $G_{p,p}$, $G_{q,q}$ (dashed, in color) and $G_{p,q}$ (solid, black) for the indicated v is computed using a periodic 48^3 mesh averaged over 30–40 independent runs (standard errors comparable to the plotting line width). Inset are illustrative snapshots of the real non-negative part of the density operators $\text{in}_p \delta \ln Q_p[\tilde{w}, \tilde{\Phi}]/\delta w(\mathbf{r})$ and $\text{in}_q \delta \ln Q_q[\tilde{w}, \tilde{\Phi}]/\delta w(\mathbf{r})$ for bead types p and q (see Supplementary Material) depicted in different colors; the component species in the same snapshot are shown separately on the side. (d) $\xi_{p,q}$ is computed using a periodic 32^3 mesh (averaged over 70–80 independent runs, solid lines) as well as the 48^3 mesh (dashed lines) used for (a–c). Error bars represents standard errors of the mean.

latter three v values are 5, 10 and 15 times the smallest $v/b^3=0.0068$, often used in FTS as a relatively poor solvent condition [21–23] favorable to LLPS [61].

PDFs indicate that significant charge pattern mismatch and strong v are both necessary for demixing. Representative results are shown in Fig. 2 (FTS details and all PDFs we computed are in the Supplementary Material). The strongest demixing is observed for sv28–sv1 with large charge pattern mismatch (SCDs differ by 15.58) at relatively high v values; e.g., for $v=0.068b^3$, $G_{\text{sv1},\text{sv28}}(r)$ takes much lower values than $G_{\text{sv1},\text{sv1}}(r)$ and $G_{\text{sv28},\text{sv28}}(r)$ as $r \rightarrow 0$ (Fig.2a), indicating that some of the sv1 chains are expelled from the sv28-dense region. Even when a single droplet is formed, it harbors sub-regions where either sv28 or sv1 dominates (snapshot in Fig.2a). However, when v decreases to $0.0068b^3$, all three G s for sv28–sv1 share similar profiles, implying that the common droplet is well mixed (Fig.2c). In contrast, for sv28–sv25 with similar charge patterns (SCDs differ by 3.22), mixing in the phase-separated droplet remains substantial even at higher v (Fig. 2b). The general trend is summarized by the mixing parameter (Fig. 2d)

$$\xi_{p,q} \equiv \frac{2\rho_p^0 \rho_q^0 G_{p,q}(0)}{(\rho_q^0)^2 G_{p,p}(0) + (\rho_p^0)^2 G_{q,q}(0)}, \quad (3)$$

which vanishes for two perfectly demixed species, because in that case at least one of the

factors in $\hat{\rho}_{b,p}(\mathbf{r})\hat{\rho}_{b,q}(\mathbf{r})$ would be zero for any \mathbf{r} , whereas $\xi_{p,q}=1$ when $\hat{\rho}_{b,p}(\mathbf{r})\propto\hat{\rho}_{b,q}(\mathbf{r})$, i.e., when the species are perfectly mixed.

MD.—While field theory affords deep physical insights, its ability to capture certain structure-related features pertinent to polyampholyte LLPS, such as the interplay between excluded volume and Coulomb interactions, can be limited [19]. Therefore, to assess the robustness of the above FTS-predicted trend, we now turn to coarse-grained explicit-chain MD for additional information.

The complete coarse-grained MD potential is given in Table I. We simulate binary mixtures of the same sv sequence pairs as with FTS, using a recently developed protocol involving initial compression and subsequent expansion of a periodic simulation box to facilitate efficient equilibrium Langevin dynamics sampling for LLPS studies [18, 19, 62]. Each of our MD systems contains 500 chains equally divided between the two sv sequences (250 chains each). The LJ parameter ϵ that governs excluded volume is set at $\epsilon=l_B/a_0$ (corresponding to the “with 1/3 LJ” prescription in [19]), $T^*\equiv(\beta\epsilon)^{-1}$ is reduced temperature, and a stiff force constant $K_b=75,000\epsilon/a_0^2$ for polymer bonds is employed as in [19, 62]. We compare results from using van der Waals radius $r_0=a_0$ (as before [19]) and $r_0=a_0/2$ to probe the effect of excluded volume. Simulations are conducted at $T^*=0.6$ and $T^*=4.0$, which is, respectively, below and above the LLPS critical temperatures of all sv sequences in Fig. 1, and at an intermediate T^* . Further details are in the Supplementary Material.

A substantive difference between common FTS and MD is in their treatment of polymer excluded volume, as illustrated in Fig. 3a for the present models, wherein $\beta V_{\text{ex}}(r)$ is the excluded-volume interaction, given by $\beta\hat{H}_1$ in Table I, for a pair of beads centered at $\mathbf{r}_{p,i,\alpha}$ and $\mathbf{r}_{q,j,\gamma}$, with $r=|\mathbf{r}_{p,i,\alpha}-\mathbf{r}_{q,j,\gamma}|$. For our FTS model as well as several recent FTS studies [21–23], $\beta V_{\text{ex}}(r)=(v/2)\int d\mathbf{r}\Gamma(\mathbf{r}-\mathbf{r}_{p,i,\alpha})\Gamma(\mathbf{r}-\mathbf{r}_{q,j,\gamma})=(v/4\pi a^2)^{3/2}\exp(-r^2/4a^2)$ is a Gaussian, which allows the beads to overlap completely ($r=0$), albeit with a reduced yet non-negligible or even moderately high probability. In contrast, for MD, $\beta V_{\text{ex}}(r)=4/3T^*[(r_0/r)^{12}-(r_0/r)^6]$, which entails a repulsive wall at $\sim r_0$ that is all but impenetrable, let alone an excluded-volume-violating complete overlap. Note that if the $\beta V_{\text{ex}}(r)$ for MD is shown for $T^*=0.2$ (as for FTS) instead of $T^*=0.6$ in Fig. 3a, the contrast would be even sharper between FTS and MD excluded-volume prescriptions.

Despite this difference, MD and FTS predictions on sequence-pattern and excluded-volume dependent population mixing/demixing upon LLPS share the same trend, and are

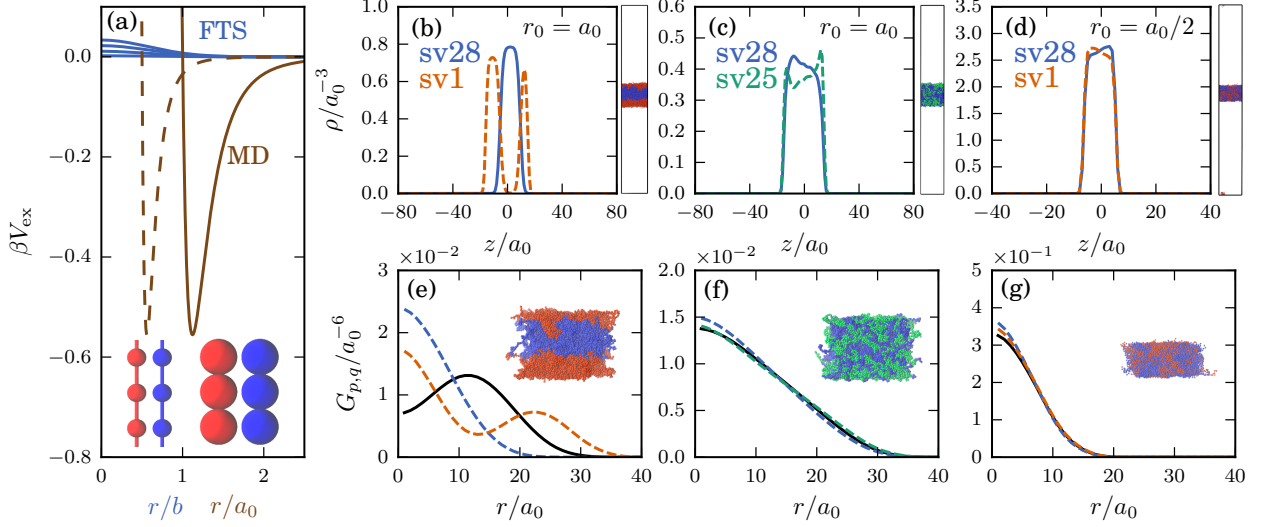


FIG. 3. MD-simulated LLPS of binary sv sequence mixtures. (a) Excluded volume interactions in FTS (blue) for $v/b^3 = 0.102, 0.068, 0.034$, and 0.0068 (top to bottom) at $T^*=0.2$ (i.e., $l_B=5b$ as in Fig. 2) and in MD (brown) for $r_0=a_0$ (solid) and $r_0=a_0/2$ (dashed) at $T^*=0.6$ (insets show relative sizes of the LJ spheres). (b)–(d) MD-simulated polyampholyte densities of binary mixtures, $\rho(z)$ s for different sv sequences are colored differently (as indicated) here and in the snapshots (on the side) of the rectangular periodic simulation boxes (wherein z is the vertical coordinate), each harboring a condensed droplet. (e)–(g) $G_{p,q}$ of the MD systems in (b)–(d), respectively, (same line style as Fig. 2a–c). Droplet snapshots (insets) are visualized [63] here with chains at periodic boundaries unwrapped.

quantitatively similar in some respects. Results for the sv28–sv1 and sv28–sv25 pairs are shown in Fig. 3b–g for $T^*=0.6$ to illustrate a perspective that is buttressed by additional MD results for other sequence pairs and other T^* in the Supplementary Material.

Fig. 3b–d show the average densities $\rho(z)$ along the long axis, z , of the rectangular simulation box. With full excluded volume and significant charge pattern mismatch, sv28 and sv1 strongly demix (cf. blue and red curves in Fig. 3b). In contrast, without a significant charge pattern mismatch, even with full excluded volume, sv28 and sv25 are quite well mixed (blue and green curves largely overlap in Fig. 3c); and, with reduced excluded volume, even sv28 and sv1 with significant charge pattern mismatch are well mixed (Fig. 3d).

This trend is echoed by the correlation functions in Fig. 3e–g, each computed from 10,000 MD snapshots. For the well-mixed cases in Fig. 3f,g, the MD-computed self ($G_{p,p}$, $G_{q,q}$) and cross ($G_{p,q}$) correlations largely overlap, similar to those in Fig. 2b,c for FTS. For the sv28–sv1 pair with full excluded volume in MD, Fig. 2e shows that $G_{p,q}(r)$ is significantly smaller than $G_{p,p}(r)$ and $G_{q,q}(r)$ for small r , as in Fig. 2a for FTS. Here, the MD $G_{q,q}$ for sv1 exhibits

a local maximum at $r \approx 23a_0$ corresponding to the distance between two sv1 density peaks in Fig. 3b. This feature reflects the anisotropic nature of the rectangular simulation box adopted to facilitate efficient sampling [62]. Nonetheless, the geometric arrangement of sv28 and sv1 in the MD system, as visualized by the snapshot in Fig. 3e, is consistent with that in Fig. 2a for FTS in that an s28-enriched core (blue) is surrounded by an sv1-enrich (red) periphery in both cases. The other MD snapshots in Fig. 3f,g depict well-mixed droplets, similar to the corresponding FTS snapshots in Fig. 2b,c.

Discussion.—Excluded volume has been shown to attenuate complex [61] and simple [22] coacervation and to promote demixing when applied differentially to molecular components in a condensate [43]. Here, FTS and MD both demonstrate a hitherto unrecognized stochastic molecular recognition principle, that a uniform excluded volume not discriminating between polymer species can nonetheless promote demixing, and that a certain threshold excluded volume is required for heteropolymers with different sequence charge patterns to demix upon LLPS. Our MD results show clearly that sequences such as sv28 and sv1 that are not obviously repulsive to each other can nevertheless demix, supporting RPA predictions that demixing of different species of overall neutral polyampholytes depends on charge pattern mismatch [46]. In light of the present finding, this success of RPA in [46] may be attributed to the incompressibility constraint—which presupposes excluded volume—in its formulation. Surprisingly, although the FTS excluded volume repulsion we consider is exceedingly weak—the highest v only amounts to $\sim 0.03k_B T$ maximum and thus can easily be overcome by thermal fluctuations (Fig. 3a), the demixing observed in FTS with this v is similar to that in MD with a much stronger, more realistic excluded volume. While the theoretical basis of this reassuring agreement, e.g., its possible relationship with the treatment of chain entropy in FTS, remains to be ascertained, our observation that sv28 and sv1 do not demix at a lower v points to potential limitations of employing small v values in FTS.

These basic principles offer new physical insights into subcompartmentalization of membraneless organelles, in terms of not only the sequence charge patterns of their constituent IDPs [46], but also of excluded volumes entailed by amino acid sidechains of various sizes, volume increases due to posttranslational modifications such as phosphorylations [64], presence of folded domains, and the solvation properties of the IDP linkers connecting these domains [2, 43]. Guided by this conceptual framework, quantitative applications to real-life biomolecular condensates require further investigations to consider sequences that are not

necessarily overall charge neutral [14], and to incorporate non-electrostatic driving forces for LLPS such as π -related [36] and hydrophobic [20, 65] interactions. Much awaits to be discovered.

We thank Yi-Hsuan Lin for insightful discussions, and gratefully acknowledge support by Canadian Institutes of Health Research grant NJT-155930, Natural Sciences and Engineering Research Council of Canada Discovery grant RGPIN-2018-04351, and computational resources of Compute/Calcul Canada.

T.P. and J.W. contributed equally to this work.

Supplementary Material

for

“Subcompartmentalization of polyampholyte species in organelle-like condensates is promoted by charge pattern mismatch and strong excluded-volume interaction”

FIELD THEORETIC SIMULATIONS

Field operators corresponding to pair distribution functions

Our target observables in the field theoretic simulations (FTS) are the pair distribution functions (PDFs), denoted as $G_{p,q}(|\mathbf{r}-\mathbf{r}'|)$ and defined in the main text in terms of the microscopic bead densities $\hat{\rho}_{b,p}(\mathbf{r})$. We show below how PDFs can be computed as ensemble averages of certain corresponding field operators in the field theoretic context. Throughout this section of Supplementary Material, we let $\langle \dots \rangle_P$ and $\langle \dots \rangle_F$ denote, respectively, averages over bead centers (i.e., in the “particle picture”) and averages over field configurations (i.e., in the “field picture”).

Using the notation in the main text, we begin by considering the canonical partition function expressed as integrals over the positions of bead centers, $\mathbf{r}_{p,i,\alpha}$, in the particle picture, with an added source field $J_p(\mathbf{r})$ for each bead type density as is commonly practiced in field theory to facilitate subsequent calculation of averages of functionals of $\hat{\rho}$:

$$Z[\{J_p\}] = \left(\prod_{p,i,\alpha} \int d\mathbf{r}_{p,i,\alpha} \right) e^{-\beta \hat{H}_0 - \beta \hat{H}_1 - \beta \hat{H}_2 + \int d\mathbf{r} \sum_p \hat{\rho}_{b,p}(\mathbf{r}) J_p(\mathbf{r})}. \quad (\text{S1})$$

To avoid notational clutter, overall multiplicative constant factors in Z that are immaterial to the quantities computed in this work are not included in the mathematical expressions in the present derivation. Using Eq. (S1), averages of products of bead densities can formally be computed using functional derivatives of Z with respect to the source fields J_p , then followed by setting $J_p=0$ for all p . In particular,

$$G_{p,q}(|\mathbf{r}-\mathbf{r}'|) \equiv \langle \hat{\rho}_{b,p}(\mathbf{r}) \hat{\rho}_{b,q}(\mathbf{r}') \rangle_P = \lim_{J_p, J_q \rightarrow 0} \frac{1}{Z} \frac{\delta}{\delta J_p(\mathbf{r})} \frac{\delta}{\delta J_q(\mathbf{r}')} Z. \quad (\text{S2})$$

We may now turn Eq. (S1) into a statistical field theory (see, e.g., Ref. [55] for detailed formulation) while still keeping the source fields. To this end, without loss of generality, we

first multiply the right hand side of (from the left) by unity ('1') in the form of

$$1 = \int \mathcal{D}\rho_b(\mathbf{r}) \delta[\rho_b - \hat{\rho}_b] \int \mathcal{D}\rho_c(\mathbf{r}) \delta[\rho_c - \hat{\rho}_c],$$

after which we can make the replacements $\hat{\rho}_{b,c} \rightarrow \rho_{b,c}$ in $\beta \hat{H}_{1,2}$ because of the δ -functionals, which are then expressed in their equivalent Fourier forms,

$$\delta[\rho_b - \hat{\rho}_b] = \int \mathcal{D}w(\mathbf{r}) e^{i \int d\mathbf{r} w(\rho_b - \hat{\rho}_b)}, \quad \delta[\rho_c - \hat{\rho}_c] = \int \mathcal{D}\Phi(\mathbf{r}) e^{i \int d\mathbf{r} \Phi(\rho_c - \hat{\rho}_c)},$$

where $i^2 = -1$, to allow for an explicit functional integrals over the $\rho_b(\mathbf{r})$ and $\rho_c(\mathbf{r})$ variables introduced by the above '1' factor. Up to a multiplicative constant, the result of those integrations is the formula

$$Z[\{J_p\}] = \int \mathcal{D}w(\mathbf{r}) \int \mathcal{D}\Phi(\mathbf{r}) \exp \left[\sum_p n_p \ln Q_p[i\check{w} - \check{J}_p, i\check{\Phi}] - \int d\mathbf{r} \left(\frac{w^2}{2v} + \frac{(\nabla \Phi)^2}{8\pi l_B} \right) \right], \quad (\text{S3})$$

where $\check{w}(\mathbf{r}) = \Gamma \star w(\mathbf{r}) \equiv \int d\mathbf{r}' \Gamma(\mathbf{r} - \mathbf{r}') w(\mathbf{r}')$ with $\Gamma(\mathbf{r}) = \exp(-\mathbf{r}^2/2a^2)/(2\pi a^2)^{3/2}$ being the unit-normalized Gaussian distribution used to model a single bead centered at position \mathbf{r} , as discussed in the main text. In Eq. (S3), the single-polymer partition function for a chain of type p is defined as

$$Q_p[i\check{w} - \check{J}_p, i\check{\Phi}] \equiv \left(\prod_{\alpha=1}^{N_p} \int d\mathbf{r}_\alpha \right) \exp \left[-\frac{3}{2b^2} \sum_{\alpha=1}^{N_p-1} (\mathbf{r}_{\alpha+1} - \mathbf{r}_\alpha)^2 - \sum_{\alpha=1}^{N_p} \left(i\check{w}(\mathbf{r}_\alpha) - \check{J}(\mathbf{r}_\alpha) + i\sigma_{p,\alpha} \check{\Phi}(\mathbf{r}_\alpha) \right) \right],$$

where N_p is the number of beads in a polymer of type p . The foregoing steps put us in a position to derive field operators whose ensemble averages correspond to the PDFs. Consider now the field operator

$$\tilde{\rho}_{b,p}(\mathbf{r}) \equiv \lim_{J_p \rightarrow 0} n_p \frac{\delta \ln Q_p[i\check{w} - \check{J}_p, i\check{\Phi}]}{\delta J_p(\mathbf{r})} = i n_p \frac{\delta \ln Q_p[i\check{w}, i\check{\Phi}]}{\delta w(\mathbf{r})},$$

so named ($\sim \rho$) because $\langle \tilde{\rho}_{b,p}(\mathbf{r}) \rangle_F = \langle \hat{\rho}_{b,p}(\mathbf{r}) \rangle_P$. [Incidentally, this ensemble average is easily computed by exploiting the translation invariance of the model. Since $\langle \hat{\rho}_{b,p}(\mathbf{r}) \rangle_P = \langle \hat{\rho}_{b,p}(\mathbf{r} + \mathbf{a}) \rangle_P$ for any \mathbf{a} , $\langle \hat{\rho}_{b,p}(\mathbf{r}) \rangle_P = \int d\mathbf{r} \langle \hat{\rho}_{b,p}(\mathbf{r}) \rangle_P / V = \langle \int d\mathbf{r} \hat{\rho}_{b,p}(\mathbf{r}) \rangle_P / V = n_p N_p / V$, where V is system volume. The last equality holds because $\int d\mathbf{r} \hat{\rho}_{b,p}(\mathbf{r}) = n_p N_p$ holds identically.] Nonetheless, it should be emphasized that the correspondence between this field operator and real-space bead density exists only at the level of their respective ensemble averages. Although individual spatial configurations of the real part [66] of $\tilde{\rho}_{b,p}(\mathbf{r})$ that is non-negative are highly suggestive and qualitatively consistent with the rigorous conclusions from PDFs (Fig. 2 in the main text), strictly speaking one cannot interpret $\tilde{\rho}_{b,p}(\mathbf{r})$ in terms of the actual

bead positions for any single field configuration $\{w(\mathbf{r}), \Phi(\mathbf{r})\}$.

We then compute $Q_p[i\check{w}, i\check{\Phi}]$ and $\tilde{\rho}_{b,p}(\mathbf{r})$ using so-called forward- and backward chain propagators $q_{F,p}(\mathbf{r}, \alpha)$ and $q_{B,p}(\mathbf{r}, \alpha)$, constructed iteratively using the Chapman-Kolmogorov equations

$$\begin{aligned} q_{F,p}(\mathbf{r}, \alpha+1) &= e^{-i\check{w}(\mathbf{r}) - i\sigma_{p,\alpha+1}\check{\Phi}(\mathbf{r})} \int d\mathbf{r}' e^{-3(\mathbf{r}-\mathbf{r}')^2/2b^2} q_{F,p}(\mathbf{r}', \alpha), \\ q_{B,p}(\mathbf{r}, \alpha-1) &= e^{-i\check{w}(\mathbf{r}) - i\sigma_{p,\alpha-1}\check{\Phi}(\mathbf{r})} \int d\mathbf{r}' e^{-3(\mathbf{r}-\mathbf{r}')^2/2b^2} q_{B,p}(\mathbf{r}', \alpha), \end{aligned}$$

while starting from $q_{F,p}(\mathbf{r}, 1) = \exp[-i\check{w}(\mathbf{r}) - i\sigma_{p,1}\check{\Phi}(\mathbf{r})]$ and $q_{B,p}(\mathbf{r}, N_p) = \exp[-i\check{w}(\mathbf{r}) - i\sigma_{p,N_p}\check{\Phi}(\mathbf{r})]$. With $q_{F,p}$ and $q_{B,p}$ in place, we arrive at

$$Q_p[i\check{w}, i\check{\Phi}] = \int d\mathbf{r} q_{F,p}(\mathbf{r}, N_p) \quad \text{and} \quad \tilde{\rho}_{b,p}(\mathbf{r}) = \Gamma \star \frac{1}{Q_p[i\check{w}, i\check{\Phi}]} \sum_{\alpha=1}^{N_p} q_{F,p}(\mathbf{r}, \alpha) q_{B,p}(\mathbf{r}, \alpha) e^{i\check{w}(\mathbf{r}) + i\sigma_{p,\alpha}\check{\Phi}(\mathbf{r})}.$$

For inter-species PDF, i.e., $G_{p,q}(|\mathbf{r}-\mathbf{r}'|)$ with $p \neq q$, Eq. (S2) applied to Eq. (S3) leads directly to

$$G_{p,q}(|\mathbf{r}-\mathbf{r}'|) = \langle \tilde{\rho}_{b,p}(\mathbf{r}) \tilde{\rho}_{b,q}(\mathbf{r}') \rangle_F, \quad p \neq q.$$

A direct application of Eq. (S2) to obtain the intra-species PDF $G_{p,p}(|\mathbf{r}-\mathbf{r}'|)$ is also possible; but that procedure leads to an expression containing a double functional derivative, viz., $\sim \delta^2 \ln Q_p / \delta w(\mathbf{r}) \delta w(\mathbf{r}')$, which is cumbersome to handle in numerical lattice simulations. We therefore obtain a simpler expression by performing the field redefinition $w(\mathbf{r}) \rightarrow w(\mathbf{r}) - iJ_p(\mathbf{r})$ instead before taking the second derivative. This alternate procedure results in

$$G_{p,p}(|\mathbf{r}-\mathbf{r}'|) = \frac{i}{v} \langle \tilde{\rho}_{b,p}(\mathbf{r}) w(\mathbf{r}') \rangle_F - \sum_{p \neq q} \langle \tilde{\rho}_{b,p}(\mathbf{r}) \tilde{\rho}_{b,q}(\mathbf{r}') \rangle_F.$$

That $\langle \tilde{\rho}_{b,p}(\mathbf{r}) \tilde{\rho}_{b,q}(\mathbf{r}') \rangle_F$ depends only on $|\mathbf{r}-\mathbf{r}'|$ follows from translational and rotational invariance. In practice, we use knowledge of these symmetries to make computations of the PDFs more efficient. For instance, to calculate $\langle \tilde{\rho}_{b,p}(\mathbf{r}) \tilde{\rho}_{b,q}(\mathbf{r}') \rangle_F$, we can first calculate $\langle \int d\mathbf{a} \tilde{\rho}_{b,p}(\mathbf{r}+\mathbf{a}) \tilde{\rho}_{b,q}(\mathbf{r}'+\mathbf{a}) \rangle_F / V$, which can be conveniently executed in Fourier space, with averaging over all possible directions of $\mathbf{r}-\mathbf{r}'$. In this way, we obtain manifestly translationally and rotationally invariant PDFs without spending computational time waiting for a droplet center of mass to explicitly visit all positions in the system or for a droplet to take on all possible spatial orientations. In the calculation of $G_{p,q}(|\mathbf{r}-\mathbf{r}'|)$ from lattice configurations, $|\mathbf{r}-\mathbf{r}'|$ is taken to be the shortest distance between positions \mathbf{r} and \mathbf{r}' with periodic boundary conditions taken into account.

Lattice simulation and sequence-, excluded-volume-, and temperature-dependent results

FTS in the present study is performed on 32^3 and 48^3 lattices (meshes) with periodic boundary conditions and side-length $V^{1/3}=13.88b$ and $V^{1/3}=24.0b$, respectively. The Complex-Langevin (CL) evolution equations are integrated from random initial conditions using a step size $\Delta t=0.001b^3$ in CL time for the 32^3 mesh, and $\Delta t=0.0005b^3$ in CL time for the 48^3 mesh, with a Gaussian noise η_φ satisfying $\langle \eta_\varphi(\mathbf{r},t) \rangle = 0$ and $\langle \eta_\varphi(\mathbf{r},t) \eta_\varphi(\mathbf{r}',t') \rangle = 2\delta(\mathbf{r}-\mathbf{r}')\delta(t-t')$. After an initial equilibration period of 40,000 steps, the systems are sampled every 1,000 steps until a total of $\sim 1,000$ sample field configurations are obtained for each run. These field configurations are used in the averages described above. For each binary sequence mixture and excluded-volume strength v , ~ 80 and ~ 40 independent runs are performed, respectively, for the 32^3 and 48^3 systems.

Figs. S1 and S2 show PDFs of sv sequence pairs computed using, respectively, the 32^3 and 48^3 meshes under various excluded volume strengths v . Results are available for the highest $v/b^3=0.102$ we simulated for the 32^3 mesh but not for the 48^3 mesh because equilibration is problematic for the larger mesh at strong excluded volume. As discussed in the main text, at the low temperature ($l_B=5b$, $T^*=0.2$) at which these simulations are conducted, a hallmark for the existence of a condensed droplet is the decay of the $G_{p,p}$, $G_{q,q}$, and $G_{p,q}$ functions to ≈ 0 at $r \approx 10b$; and a significant demixing of the populations of the two sequence species is signaled by a substantially lower $G_{p,q}(r)$ ($p \neq q$), for small $r \approx 0$, than both $G_{p,p}(r)$ and $G_{q,q}(r)$ in the same range of r . The trends exhibited by the two sets of results in Figs. S1 and S2 are consistent. They indicate robustly that both a significant difference in sequence charge pattern of the two polyampholyte species (difference decreases from the sv28-sv1 to the sv28-sv25 pair) and a substantial excluded volume (relatively large v values) are required for appreciable demixing. This observation corroborates the trend illustrated by the sv28-sv1 and sv28-sv25 examples and the $\xi_{p,q}$ measure presented in Fig. 2 of the main text. As a control, and not surprisingly, when FTS is conducted at a much higher temperature of $T^*=20$ ($l_B=0.05b$) in Fig. S3, there is little sequence dependence—as seen by the very similar behaviors of all $G_{p,p}(r)$, $G_{q,q}(r)$, and $G_{p,q}(r)$ among the sequence pairs considered—and there is no droplet formation. Instead of converging to zero at large r as in Figs. S1 and S2, here all $G(r)$'s converge to a finite (nonzero) value of $\langle \hat{\rho}_{b,p} \rangle_P \langle \hat{\rho}_{b,q} \rangle_P \approx 0.05b^{-6}$ at large r in Fig. S3 for $p \neq q$ as well as $p = q$, signaling a total lack of correlation between bead positions that are far apart.

Illustrative snapshots of density field configurations

The dual requirements of a significant sequence charge pattern mismatch and a substantial generic excluded volume for demixing of two polyampholyte species in a condensed droplet are illustrated by the FTS snapshots for the sv28-sv1 pairs ($v/b^3=0.068$ and 0.0068) and sv28-sv25 pairs ($v/b^3=0.068$) in Fig. 2a–c of the main text. Those snapshots present an overall

view from the outside of the droplet. Thus, part of their interior structure is obscured, albeit this limitation is partly remedied by the translucent color scheme. Further analyses to better understand the internal structures of these FTS snapshots are provided by the cross-sectional views in Fig. S4. The contour plots in Fig. S4a for the sv28-sv1 system with a high generic excluded volume strength show clearly that there is indeed a three-dimensional core with highly enriched sv28 population surrounded by a shell with enriched sv1 population. In contrast, the contour plots for the sv28-sv25 system at the same excluded volume strength (Fig. S4b) and the sv28-sv1 system at a low generic excluded volume strength (Fig. S4c) indicate that the two polyampholyte species are quite well mixed in the condensed droplets of these two systems. Nonetheless, the patterns of the contours reveals that even for these well-mixed systems, sv28 is still slightly more enriched in the core and the other sv sequence is slightly more enriched in a surrounding shell region.

EXPLICIT-CHAIN COARSE-GRAINED MOLECULAR DYNAMICS (MD) SIMULATIONS

Methodological details

All MD simulations are performed using the GPU version of HOOMD-blue simulation package [67, 68] as in Ref. [19]. We initially randomly place all the polyampholyte chains inside a sufficiently large cubic simulation box of length $70a_0$. The system is then energy minimized using the inbuilt FIRE algorithm to avoid any steric contact for a period of 500τ with a timestep of 0.001τ , where $\tau \equiv \sqrt{ma^2/\epsilon}$ and m is the mass of each bead (representing a monomer, or residue). Each system is first initiated at a higher temperature—at a high $T^*=4.0$ —for a period of $5,000\tau$, where the reduced temperature $T^* \equiv k_B T/\epsilon$ (see Table I in the main text and related discussion about the MD energy scale). The box is then compressed at $T^*=4.0$ for a period of $5,000\tau$ using isotropic linear scaling until we reach a sufficiently higher density of $\sim 0.7ma_0^{-3}$ which corresponds to a box size of $33a_0 \times 33a_0 \times 33a_0$. Next, we expand the simulation box length along one of the three Cartesian directions (labeled z) 8 times compared to its initial length to reach a final box length of $33a_0 \times 33a_0 \times 264a_0$. The box expansion procedure is conducted at a sufficiently low temperature of $T^*=0.4$. After that, each system is equilibrated again at the desired temperature for a period of $30,000\tau$ using Langevin dynamics with a weak friction coefficient of $0.1m/\tau$ [62]. Velocity-Verlet algorithm is used to propagate motion with periodic boundary conditions for the simulation box. Production run is finally carried out for $100,000\tau$ and molecular trajectories are saved every 10τ for subsequent analyses. For density distribution calculations, we first adjust the periodic simulation box in such a way that its centre of mass is always at $z=0$. The simulation box is then divided along the z -axis into 264 bins of size $=a_0$ to produce a total density profile as well as profiles for the two individual polyampholyte species in the binary mixture.

Fig. S5 shows the density profiles of six sv sequence pairs (the same sv pairs analyzed using RPA in Ref. [46]). At a sufficiently low temperature of $T^*=0.6$, LLPS is observed for all systems simulated here, in that a droplet, manifested as a density plateau, is observed (left column of Fig. S5). At this low temperature, demixing of the two species in the binary mixture is clearly observed for sv28-sv1 and sv28-sv10, and nearly complete mixing is observed for sv28-sv24 and sv28-sv25. Intermediate behaviors that may be characterized as partial demixing—with sv28 slightly enriched in the middle and the other sequence species slightly enriched on the two sides—are observed for sv28-sv15 and sv28-sv20. The trend is also seen at intermediate temperatures ($T^*=1.4$ – 2.3). However, in some of these cases, one of the polyampholytes either does not (e.g. sv1) or barely (e.g. sv15) phase separate, as indicated by the long “tails” of their density profile outside the central region (middle column of Fig. S5). Not unexpectedly, at a high temperature of $T^*=4.0$, none of the simulated systems phase separates and the two species are mixed homogeneously throughout the simulation box (right column of Fig. S5). Representative snapshots of these systems are shown in Fig. S6. As for the $G_{p,q}(|\mathbf{r}-\mathbf{r}'|)$ in FTS, in the calculation of the MD-simulated $G_{p,q}(|\mathbf{r}-\mathbf{r}'|)$ from configurations in the MD simulation box with periodic boundary conditions (Fig. 3e–g of the main text), $|\mathbf{r}-\mathbf{r}'|$ is taken to be the shorter distance of the two possible inter-bead distances determined in the presence, or absence, of periodic boundary conditions.

Cross-sectional views of MD and FTS droplet structures

The MD-simulated droplet snapshots at low temperature $T^*=0.6$ in Fig. 3b–g of the main text underscore that demixing of two polyampholyte species in a condensed droplet requires a significant mismatch in sequence charge pattern as well as a substantial excluded volume repulsion. Because the beads (monomers) are represented in our MD drawings as opaque spheres, the bulk of those droplets below the surface of the image presented cannot be visualized. To better illustrate that the observed mixing/demixing trend applies not only to the exterior of the presented image of those droplets but persists in the parts underneath (as can be inferred by the behaviors of $G_{p,p}$, $G_{q,q}$, and $G_{p,q}$ in Fig. 3e–g of the main text), we prepare cut-out images of those droplets to reveal the spatial organization in their “core” regions (Fig. S7). The spatial configurations of the MD droplets and their general trend of behaviors (Fig. S7, right column) are very similar to those exhibited by cross-sectional views of FTS droplets (contour plots in Fig. S4 and density plots in Fig. S7, left column), demonstrating once again the robustness of our observations. By construction, MD provides much more spatial details than FTS in this regard. Of particular future interest is the manner in which individual positively and negatively charged beads interact across polyampholytes of different species. MD snapshots should be useful for elucidating this issue. In contrast, although FTS snapshots—with their cloudy appearances—may show a similar spatial organization of charge densities as that of MD, the field configurations do not translate into individual bead positions (Fig. S7, second row).

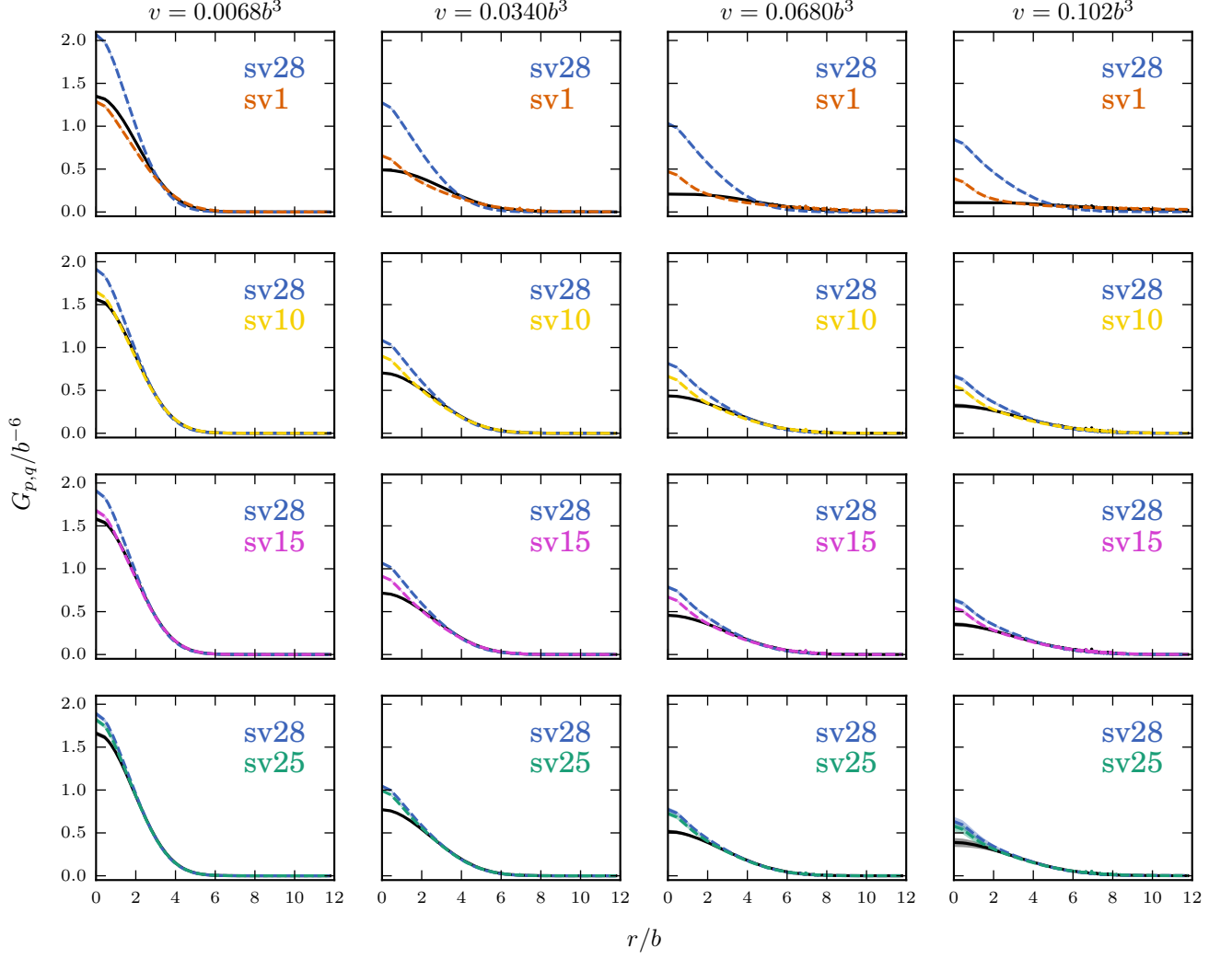


FIG. S1. PDFs of binary mixtures of sv sequences computed by FTS using a 32^3 mesh at $l_B=5b$ ($T^*=0.2$) and various v . The plotting style follows that of Fig. 2 of the main text. Dashed blue curves: $G_{p,p}(r)$ for sv28 ($-\text{SCD}=15.99$); dashed color curves: $G_{q,q}(r)$ for (top to bottom) sv1, sv10, sv15, and sv25 ($-\text{SCD}=0.41, 2.10, 4.35$, and 12.77 , respectively); solid black curves: $G_{p,q}(r)$. The shaded region around each curve represents standard error of the mean among the ~ 80 independent runs for each system, which is mostly smaller than the width of the curve.

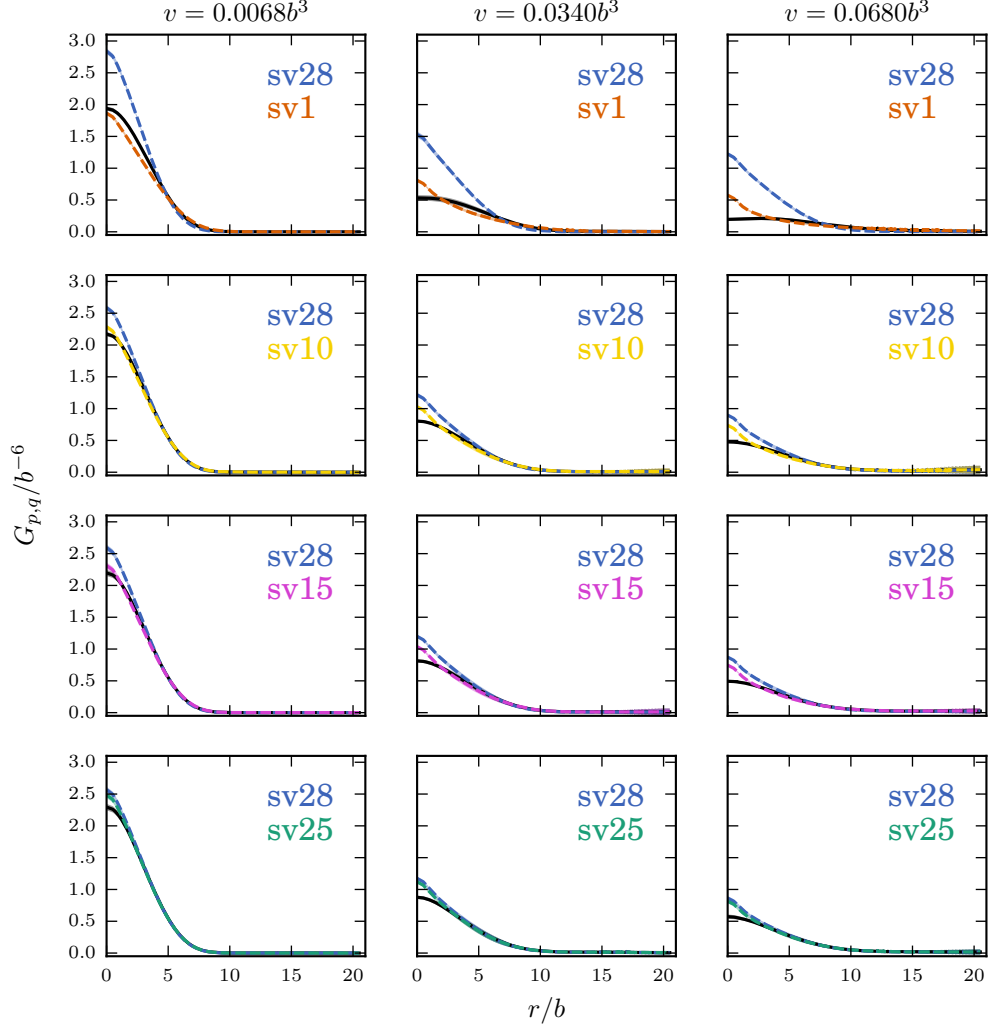


FIG. S2. PDFs of binary mixtures of sv sequences computed by FTS using a 48^3 mesh at $l_B=5b$ ($T^*=0.2$). Results for each system are from ~ 40 independent runs. The notation is otherwise the same as that of Fig. S1.

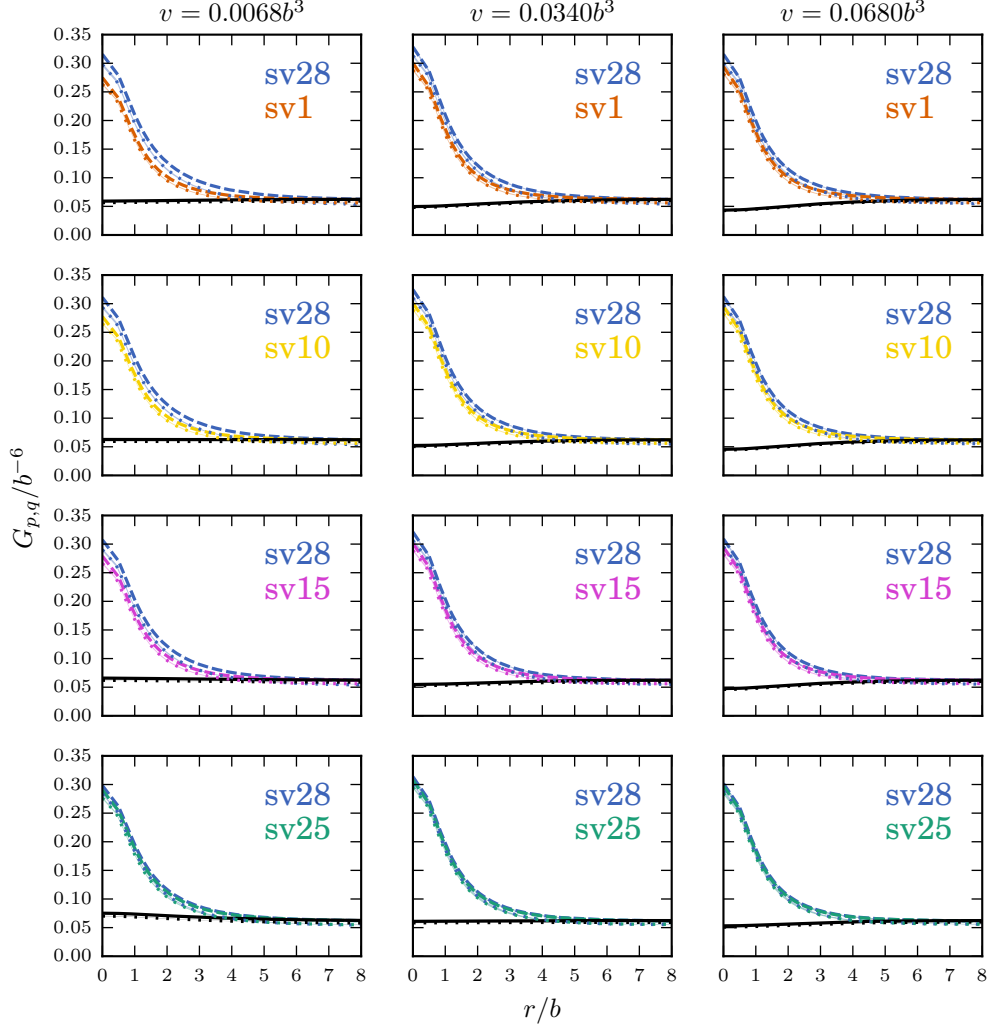


FIG. S3. PDFs of binary mixtures of sv sequences computed by FTS using a 32^3 mesh or a 48^3 mesh at $l_B=0.05b$ ($T^*=20.0$). Dashed (dotted) blue curves: $G_{p,p}(r)$ for sv28 from a 48^3 (32^3) mesh; dashed (dotted) color curves: $G_{q,q}(r)$ for (top to bottom) sv1, sv10, sv15, and sv25 from a 48^3 (32^3) mesh; solid (dotted) black curves: corresponding $G_{p,q}(r)$ obtained using a 48^3 (32^3) mesh. At this high temperature, the behaviors of all systems are very similar irrespective of the sequence charge patterns or excluded volume interaction v values considered. The r/b scale is enlarged vis-à-vis Figs. S1 and S2 to make the differences between the plotted curves here visible.

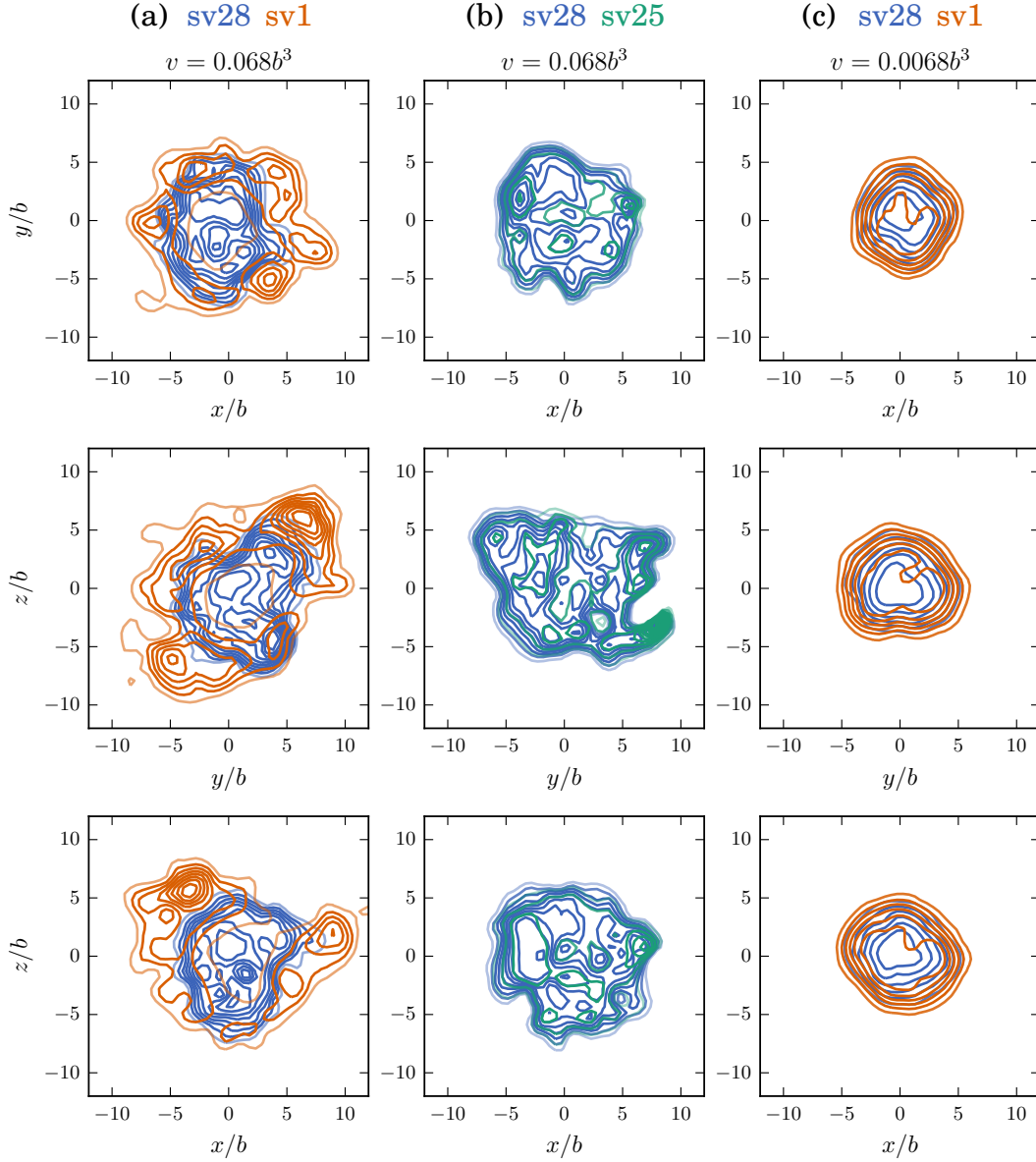


FIG. S4. Cross-sections of FTS droplets of binary sv sequence mixtures illustrating the interplaying roles of sequence charge pattern mismatch and generic excluded volume in mixing/demixing of polyampholyte species. Shown here are two-dimensional slides through the droplet center of mass in the x - y (top), y - z (middle), and x - z (bottom) planes for the three FTS droplets depicted in Fig. 2a-c of the main text. Density contours for the two sv sequence components p, q in a given mixture are color coded as indicated by the labels at the top of the (a)-(c) columns. The contours for species p (q) are curves of constant bead density, where “bead density” here in a FTS snapshot means the real non-negative part of the density operator, viz., $\Re_+(\tilde{\rho}_{b,p}(\mathbf{r})) = \Re_+(i n_p \delta \ln Q_p[i\check{w}, i\check{\Phi}]/\delta w(\mathbf{r}))$ ($\Re_+(\tilde{\rho}_{b,q}(\mathbf{r})) = \Re_+(i n_q \delta \ln Q_q[i\check{w}, i\check{\Phi}]/\delta w(\mathbf{r}))$), where $\Re_+(u) \equiv [\Re(u) + \text{sign}(\Re(u))]/2$ for any complex number u . (Among all snapshots considered, $\Re(\tilde{\rho}_{b,p}(\mathbf{r})) < -0.01b^{-3}$ occurs only for $<2\%$ of the mesh points). The contours are evenly spaced from $\Re(\tilde{\rho}_{b,p}), \Re(\tilde{\rho}_{b,q}) = 0$ [transparent] to $\Re_+(\tilde{\rho}_{b,p}) = \max\{\Re_+(\tilde{\rho}_{b,p})\}$ ($\Re_+(\tilde{\rho}_{b,q}) = \max\{\Re_+(\tilde{\rho}_{b,q})\}$) [opaque] where $\max\{\Re_+(\tilde{\rho}_{b,p})\}$ ($\max\{\Re_+(\tilde{\rho}_{b,q})\}$) is the maximum density of species p (q) in a given snapshot.

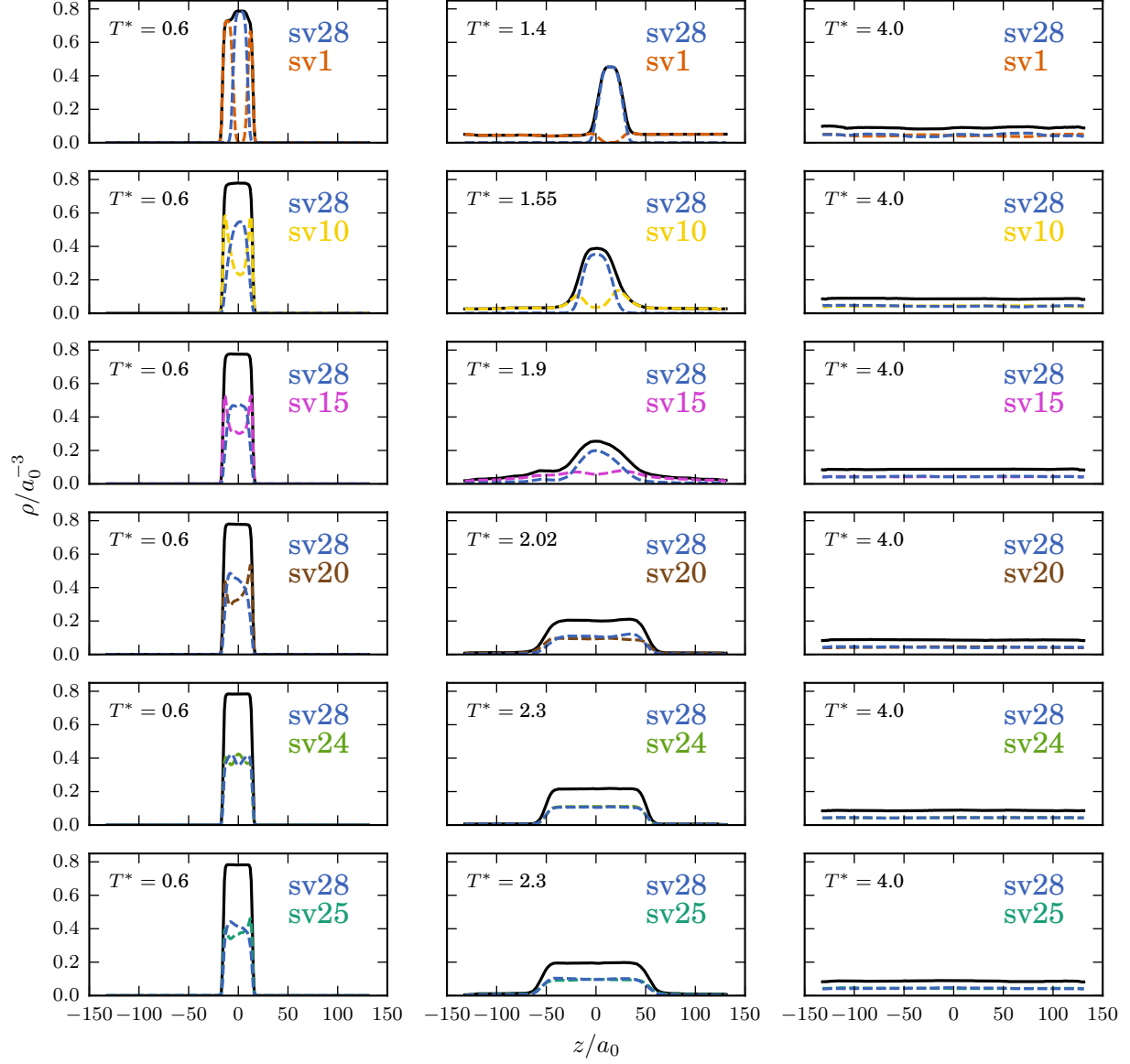
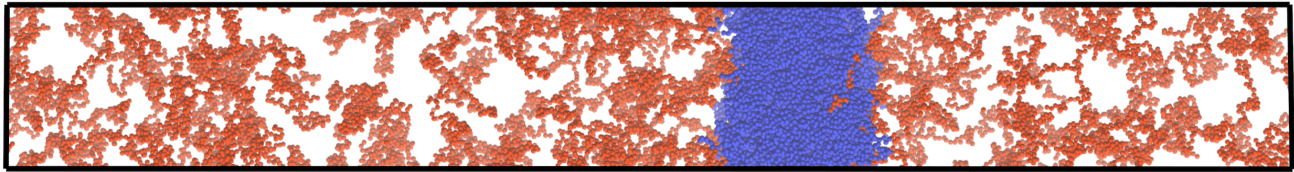
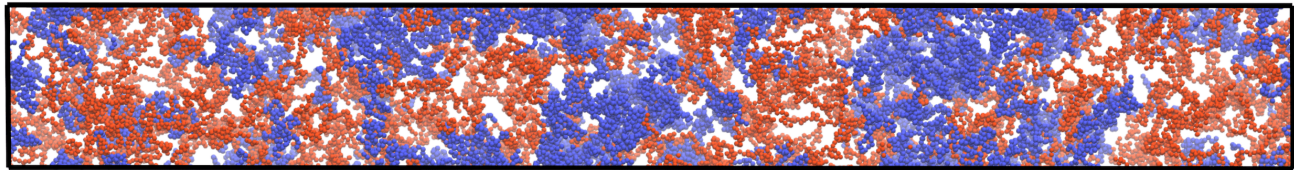


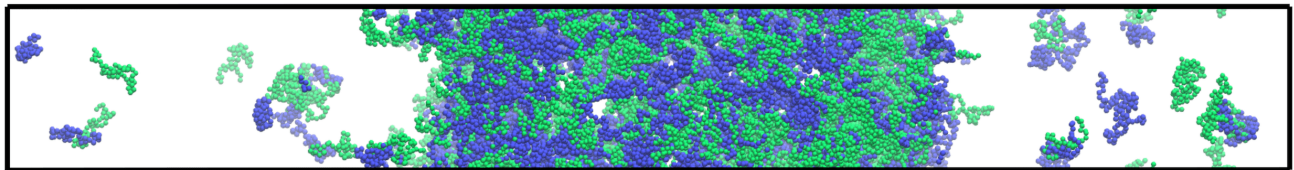
FIG. S5. MD-simulated average density of binary mixtures of sv sequences along the z (long) axis of the simulation box at various temperatures. Solid curves: total bead density; color dashed curves: density of individual sv polyampholyte species. In addition to the four sv pairs studied using FTS, MD results for the sv28-sv20 ($-\text{SCD} = 15.99, 7.37$) and sv28-sv24 ($-\text{SCD} = 15.99, 17.00$) pairs are obtained to cover the six sv pairs studied using RPA [46].



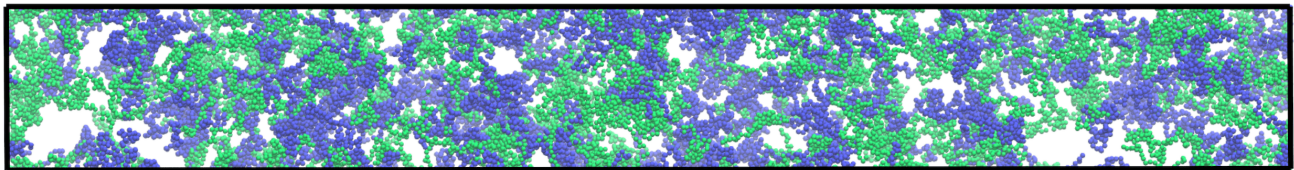
(a) sv28-sv1, $T^*=1.4$



(b) sv28-sv1, $T^*=4.0$



(c) sv28-sv25, $T^*=2.3$



(d) sv28-sv25, $T^*=4.0$

FIG. S6. Simulation snapshots of binary mixtures of sv sequences at the reduced temperatures indicated. Polyampholyte chains with charge sequences sv28, sv1, and sv25 are depicted, respectively, in blue, red, and green.

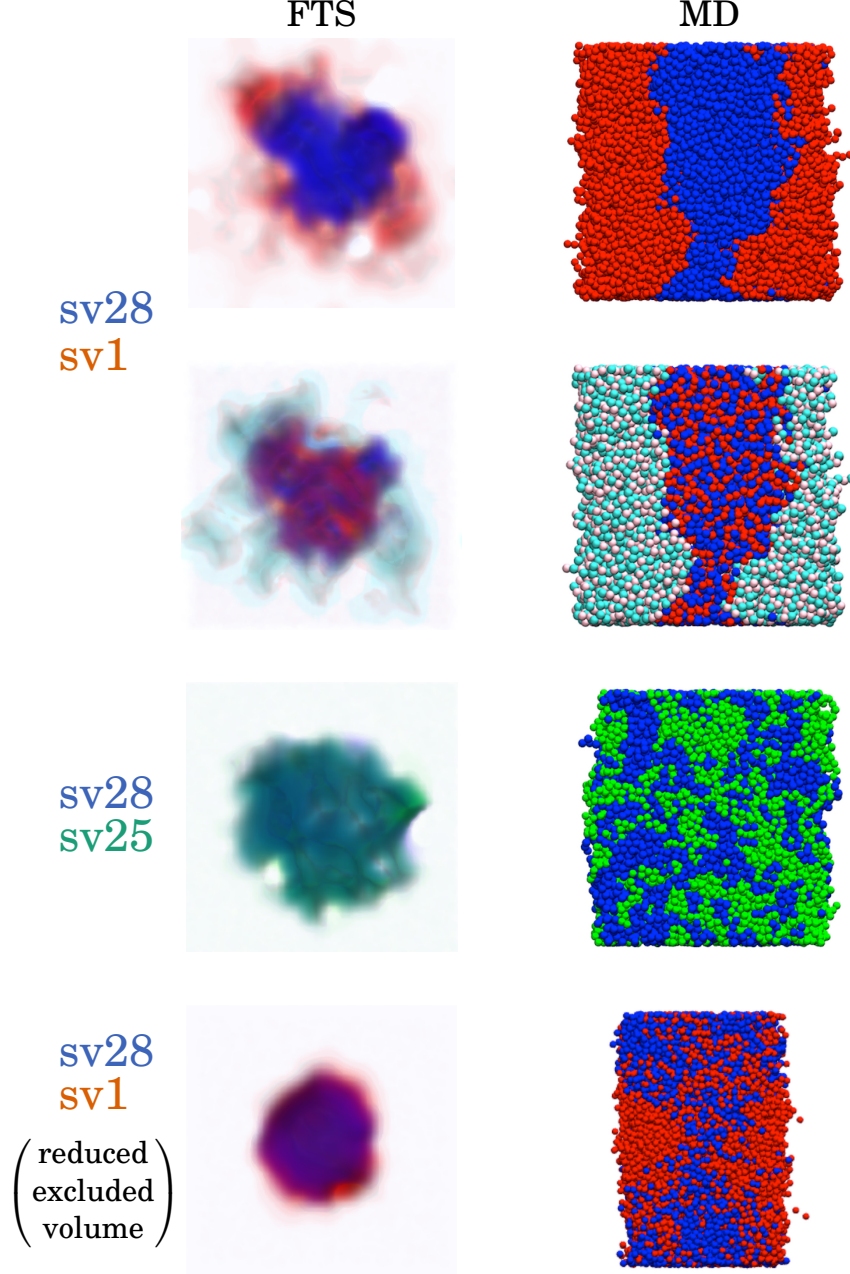


FIG. S7. Cross-sectional views of FTS and MD snapshots of binary mixtures of polyampholytes afford a consistent picture of sequence- and excluded-volume-dependent droplet organization. (Left) FTS density distributions on one of the two-dimensional planes in Fig. S4 through each droplet's center of mass. (Right) Corresponding cut-out views of the MD droplets shown inside the periodic simulation boxes in Fig. 3b–d of the main text at one half of the box dimension extending perpendicularly into the page. Two different representations are used to visualize the sv28-sv1 droplet with full excluded volume (top two rows; $v=0.068b^3$, $r_0=a_0$). Upper row: sv1 and sv28 are depicted, respectively, in red and blue. Lower row: The negatively and positively charged beads in sv28 are depicted, respectively, in red and blue, whereas the corresponding beads in sv1 are depicted in pink and cyan. The color code for the sv28-sv25 mixture at full excluded volume (third row from top; $v=0.068b^3$, $r_0=a_0$) and the sv28-sv1 mixture with reduced excluded volume (bottom row; $v=0.0068b^3$, $r_0=a_0/2$) follows that in Figs. 2 and 3 of the main text.

* chan@arrhenius.med.utoronto.ca

- [1] C. P. Brangwynne, C. R. Eckmann, D. S. Courson, A. Rybarska, C. Hoege, J. Gharakhani, F. Jülicher, and A. A. Hyman, *Science* **324**, 1729 (2009).
- [2] P. Li, S. Banjade, H. C. Cheng, S. Kim, B. Chen, L. Guo, M. Llaguno, J. V. Hollingsworth, D. S. King, S. F. Banani, P. S. Russ, Q.-X. Jiang, B. T. Nixon, and M. K. Rosen, *Nature* **483**, 336 (2012).
- [3] M. Kato, T. W. Han, S. Xie, K. Shi, X. Du, L. C. Wu, H. Mirzaei, E. J. Goldsmith, J. Longgood, J. Pei, N. V. Grishin, D. E. Frantz, J. W. Schneider, S. Chen, L. Li, M. R. Sawaya, D. Eisenberg, R. Tycko, and S. L. McKnight, *Cell* **149**, 753 (2012).
- [4] A. A. Hyman, C. A. Weber, and F. Jülicher, *Annu. Rev. Cell Dev. Biol.* **30**, 39 (2014).
- [5] T. J. Nott, E. Petsalaki, P. Farber, D. Jervis, E. Fussner, A. Plochowietz, T. D. Craggs, D. P. Bazett-Jones, T. Pawson, J. D. Forman-Kay, and A. J. Baldwin, *Mol. Cell* **57**, 936 (2015).
- [6] S. F. Banani, H. O. Lee, A. A. Hyman, and M. K. Rosen, *Nat. Rev. Mol. Cell. Biol.* **18**, 285 (2017).
- [7] S. Alberti, *Curr. Biol.* **27**, R1097 (2017).
- [8] A. Molliex, J. Temirov, J. Lee, M. Coughlin, A. P. Kanagaraj, H. J. Kim, T. Mittag, and J. P. Taylor, *Cell* **163**, 123 (2015).
- [9] X.-H. Li, P. L. Chavali, R. Pancsa, S. Chavali, and M. M. Babu, *Biochemistry* **57**, 2452 (2018).
- [10] T. Chen, J. Song, and H. S. Chan, *Curr. Opin. Struct. Biol.* **30**, 32 (2015).
- [11] C. P. Brangwynne, P. Tompa, and R. V. Pappu, *Nat. Phys.* **11**, 899 (2015).
- [12] Y.-H. Lin, J. D. Forman-Kay, and H. S. Chan, *Phys. Rev. Lett.* **117**, 178101 (2016).
- [13] L.-W. Chang, T. K. Lytle, M. Radhakrishna, J. J. Madinya, J. Vélez, C. E. Sing, and S. L. Perry, *Nat. Comm.* **8**, 1273 (2017).
- [14] Y.-H. Lin, J. P. Brady, H. S. Chan, and K. Ghosh, *J. Chem. Phys.* **152**, 045102 (2020).
- [15] M. Feric, N. Vaidya, T. S. Harmon, D. M. Mitrea, L. Zhu, T. M. Richardson, R. W. Kriwacki, R. V. Pappu, and C. P. Brangwynne, *Cell* **165**, 1686 (2016).
- [16] S. Das, A. Eisen, Y.-H. Lin, and H. S. Chan, *J. Phys. Chem. B* **122**, 5418 (2018).
- [17] J.-M. Choi, F. Dar, and R. V. Pappu, *PLoS Comput. Biol.* **15**, 1 (2019).
- [18] G. L. Dignon, W. Zheng, Y. C. Kim, R. B. Best, and J. Mittal, *PLoS Comput. Biol.* **14**,

- e1005941 (2018).
- [19] S. Das, A. N. Amin, Y.-H. Lin, and H. S. Chan, *Phys. Chem. Chem. Phys.* **20**, 28558 (2018).
 - [20] A. Statt, H. Casademunt, C. P. Brangwynne, and A. Z. Panagiotopoulos, *J. Chem. Phys.* **152**, 075101 (2020).
 - [21] Y. Lin, J. McCarty, J. N. Rauch, K. T. Delaney, K. S. Kosik, G. H. Fredrickson, J.-E. Shea, and S. Han, *eLife* **8**, e42571 (2019).
 - [22] J. McCarty, K. T. Delaney, S. P. O. Danielsen, G. H. Fredrickson, and J.-E. Shea, *J. Phys. Chem. Lett.* **10**, 1644 (2019).
 - [23] S. P. O. Danielsen, J. McCarty, J.-E. Shea, K. T. Delaney, and G. H. Fredrickson, *Proc. Natl. Acad. Sci. U. S. A.* **116**, 8224 (2019).
 - [24] Y.-H. Lin and H. S. Chan, *Biophys. J.* **112**, 2043 (2017).
 - [25] G. L. Dignon, W. Zheng, R. B. Best, Y. C. Kim, and J. Mittal, *Proc. Natl. Acad. Sci. U. S. A.* **115**, 9929 (2018).
 - [26] N. A. S. Robichaud, I. Saika-Voivod, and S. Wallin, *Phys. Rev. E* **100**, 052404 (2019).
 - [27] G. L. Dignon, W. Zheng, Y. C. Kim, and J. Mittal, *ACS Cent. Sci.* **5**, 821 (2019).
 - [28] H. Cinar, R. Oliva, Y.-H. Lin, X. Chen, M. Zhang, H. S. Chan, and R. Winter, *Chem Eur. J.* **26**, doi:10.1002/chem.201905269 (2020).
 - [29] D. Nilsson and A. Irback, *Phys. Rev. E* **101**, 022413 (2020).
 - [30] Y.-H. Lin, J. D. Forman-Kay, and H. S. Chan, *Biochemistry* **57**, 2499 (2018).
 - [31] G. L. Dignon, W. Zheng, and J. Mittal, *Curr. Opin. Chem. Eng.* **23**, 92 (2019).
 - [32] H. Cinar, Z. Fetahaj, S. Cinar, R. M. Vernon, H. S. Chan, and R. Winter, *Chem. Eur. J.* **57**, 13049 (2019).
 - [33] J.-M. Choi, A. S. Holehouse, and R. V. Pappu, *Annu. Rev. Biophys.* **49**, doi: 10.1146/annurev (2020).
 - [34] C. E. Sing and S. L. Perry, *Soft Matter* **16**, 2885 (2020).
 - [35] V. N. Uversky, *Protein Sci.* **11**, 739 (2002).
 - [36] R. M. Vernon, P. A. Chong, B. Tsang, T. H. Kim, A. Bah, P. Farber, H. Lin, and J. D. Forman-Kay, *eLife* **7**, e31486 (2018).
 - [37] R. K. Das and R. V. Pappu, *Proc. Natl. Acad. Sci. U. S. A.* **110**, 13392 (2013).
 - [38] L. Sawle and K. Ghosh, *J. Chem. Phys.* **143**, 085101 (2015).
 - [39] J. Huihui and K. Ghosh, *J. Chem. Phys.* **152**, 161102 (2020).

- [40] M. Thiry and D. L. Lafontaine, Trends Cell Biol. **15**, 194 (2005).
- [41] P. A and S. C. Weber, Noncoding RNA **5**, 50 (2019).
- [42] S. Jain, J. R. Wheeler, R. W. Walters, A. Agrawal, A. Barsic, and R. Parker, Cell **164**, 487 (2016).
- [43] Y. S. Harmon, A. S. Holehouse, and R. V. Pappu, New J. Phys. **20**, 045002 (2018).
- [44] W. M. Jacobs and D. Frenkel, Biophys. J. **112**, 683 (2017).
- [45] A. V. Ermoshkin and M. Olvera de la Cruz, Macromolecules **36**, 7824 (2003).
- [46] Y.-H. Lin, J. P. Brady, J. D. Forman-Kay, and H. S. Chan, New J. Phys. **19**, 115003 (2017).
- [47] H. S. Chan and K. A. Dill, Proc. Natl. Acad. Sci. U. S. A. **87**, 6388 (1990).
- [48] A. Maritan, C. Micheletti, A. Trovato, and J. R. Banavar, Nature **406**, 287 (2000).
- [49] S. Wallin and H. S. Chan, Protein Sci. **14**, 1643 (2005).
- [50] S. Wallin and H. S. Chan, J. Phys.: Condens. Matter **18**, S307 (2006).
- [51] J. Song, G.-N. Gomes, C. C. Gradinaru, and H. S. Chan, J. Phys. Chem. B **119**, 15191 (2015).
- [52] S. F. Edwards, Proc. Phys. Soc. **85**, 613 (1965).
- [53] R. A. Riggleman, R. Kumar, and G. H. Fredrickson, J. Chem. Phys. **136**, 024903 (2012).
- [54] Z.-G. Wang, Phys. Rev. E **81**, 021501 (2010).
- [55] G. H. Fredrickson, *The Equilibrium Theory of Inhomogeneous Polymers* (Oxford University Press, Oxford, U.K., 2006).
- [56] G. Parisi and Y.-S. Wu, Sci. Sinica **24**, 483 (1981).
- [57] G. Parisi, Phys. Lett. B **131**, 393 (1983).
- [58] J. R. Klauder, J. Phys. A: Math. Gen. **16**, L317 (1983).
- [59] H. S. Chan and M. B. Halpern, Phys. Rev. D **33**, 540 (1986).
- [60] E. M. Lennon, G. O. Mohler, H. D. Ceniceros, C. J. García-Cervera, and G. H. Fredrickson, Multiscale Model. Simul. **6**, 1347 (2008).
- [61] S. L. Perry and C. E. Sing, Macromolecules **48**, 5040 (2015).
- [62] K. S. Silmore, M. P. Howard, and A. Z. Panagiotopoulos, Mol. Phys. **115**, 320 (2017).
- [63] W. Humphrey, A. Dalke, and K. Schulten, J. Mol. Graphics **14**, 33 (1996).
- [64] T. H. Kim, B. Tsang, R. M. Vernon, N. Sonenberg, L. E. Kay, and J. D. Forman-Kay, Science **365**, 825 (2019).
- [65] W. Zheng, G. Dignon, M. Brown, Y. C. Kim, and J. Mittal, J. Phys. Chem. Lett. **11**, 3408 (2020).

- [66] G. H. Fredrickson, V. Ganesan, and F. Drolet, *Macromolecules* **35**, 16 (2002).
- [67] J. Anderson, C. Lorenz, and A. Travesset, *J. Comput. Phys.* **227**, 5342 (2008).
- [68] J. Glaser, T. D. Nguyen, J. A. Anderson, P. Lui, F. Spiga, J. A. Millan, D. C. Morse, and S. C. Glotzer, *Comput. Phys. Comm.* **192**, 97 (2015).